Earth and Space Science

RESEARCH ARTICLE
10.1029/2019EA000915

Mid-Infrared Optical Constants of Labradorite, a Triclinic Plagioclase Mineral

Cheng Ye[1], Melinda J. Rucks[1,2], Jessica A. Arnold[3], and Timothy D. Glotch[1]

[1]Department of Geosciences, Stony Brook University, Stony Brook, NY, USA, [2]Department of Geosciences, Princeton University, Princeton, NJ, USA, [3]Department of Terrestrial Magnetism, Carnegie Institution for Science, Washington, DC, USA

Key Points:
- Mid-infrared spectroscopy is an effective tool to detect plagioclase from remote sensing data sets
- We have derived the mid-infrared oriented optical constants of a triclinic rock-forming plagioclase mineral, labradorite
- The averaged optical constants acquired from contributions of each principal axis can be used to model spectra by radiative transfer theory

Correspondence to:
C. Ye,
cheng.ye.1@stonybrook.edu

Citation:
Ye, C., Rucks, M. J., Arnold, J. A., & Glotch, T. D. (2019). Mid-Infrared Optical Constants of Labradorite, a Triclinic Plagioclase Mineral. *Earth and Space Science*, *6*, 2410–2422. https://doi.org/10.1029/2019EA000915

Received 2 OCT 2019
Accepted 15 NOV 2019
Accepted article online 4 DEC 2019
Published online 14 DEC 2019

©2019. The Authors.
This is an open access article under the terms of the Creative Commons Attribution-NonCommercial-NoDerivs License, which permits use and distribution in any medium, provided the original work is properly cited, the use is non-commercial and no modifications or adaptations are made.

Abstract Plagioclase feldspar is the most abundant rock-forming mineral in the crust of the Earth, Moon, and Mars and is also an important component in some minor bodies in the Solar System. The distribution, abundance, and precise composition of plagioclase on planetary surfaces from remote sensing data are important measurements for evaluating changing conditions during magma evolution. Optical constants are critical input parameters in radiative transfer theory, which enables modeling of spectra for the extraction of mineral abundances and grain sizes from a remotely sensed spectrum. Mid-infrared (MIR) optical constants of most triclinic rock-forming minerals are not available due to the complexity associated with the derivation of optical constants of low-symmetry minerals. In this work, we have calculated the MIR optical constants of a labradorite single crystal using dispersion theory and laboratory reflectance spectra at non-normal incidence. The optical constants we derived here will assist in modeling spectra in the MIR region and quantifying mineral composition, particle size, and abundances from remote sensing data.

1. Introduction

Plagioclase is the one of the most common rock-forming minerals on the Earth, Moon, Mars, and some asteroids in the Solar System. Plagioclase consists a series of compositions from albite ($NaAlSi_3O_8$) to anorthite ($CaAl_2Si_2O_8$) that indicate changing conditions during fractional crystallization. Remote identification of plagioclase is difficult at visible and near-infrared (VNIR, 0.35–2.5 μm) wavelengths due to the lack of diagnostic absorption features in this spectral region, although usually there is a broad band at about 1.25 μm caused by minor amounts of Fe^{2+} in the plagioclase crystal structure (Adams & Goullaud, 1978). This band, however, is easily masked by <15 vol.% of mafic phases, such as pyroxene or olivine (Crown & Pieters, 1987; Nash & Conel, 1974). On the Moon, VNIR spectroscopy has been used to identify pure plagioclase using this feature only in areas that lack mafic phases (Cheek et al., 2013; Donaldson Hanna et al., 2014).

Mid-infrared (MIR, ~5–50 μm or ~2,000–200 cm^{-1}) spectroscopy is an effective tool to detect plagioclase from remote sensing data sets because plagioclase minerals have distinct, fundamental spectral signatures in the MIR region. The shapes and positions of bands in the MIR and the wavelength position of the Christiansen Feature, the emissivity maximum, provide unique characteristics that distinguishes plagioclase composition varying from albite to anorthite (Nash & Salisbury, 1991; Salisbury et al., 1991). Qualitative identification and quantitative extraction of the distribution, type, and abundance of plagioclase minerals on planetary surfaces from remote sensing data are critical to better understand the magmatic evolution of the planets. In order to quantify the mineral composition from MIR spectra, simple linear least squares models are appropriate for cases in which the grain size is larger than the wavelength of light (e.g., Ramsey & Christensen, 1998). For finely particulate surfaces (compared to the wavelength of light), spectral mixing is nonlinear, and radiative transfer theory must be used to model the light interaction processes with minerals that control spectral features. Optical constants (n and k, the real and imaginary parts of the complex index of refraction, respectively), which are dependent on the fundamental structural and chemical properties of minerals, are important input parameters in the light scattering models used to extract mineral abundances of planetary surfaces.

At MIR wavelengths, classical Lorentz-Lorenz dispersion theory combined with a Fresnel reflectance model is widely used to derive optical constants of isotropic materials. This method can also be used on uniaxial

crystals and the orthorhombic system of biaxial crystals with polarized light applied, because the symmetry elements of the crystal structure are perpendicular to each other, and the principle axes are parallel to the crystallographic axes. Therefore, the optical constants derived with success are mostly focused on orthorhombic and higher symmetry materials (e.g., quartz, Spitzer & Kleinman, 1961; Wenrich & Christensen, 1996; calcite, Lane, 1999; iron oxides, Glotch et al., 2006; Glotch & Rossman, 2009; orthopyroxenes, Rucks & Glotch, 2014).

However, the application of dispersion theory to derive optical constants of non-orthogonal systems of anisotropic crystals in the monoclinic and triclinic crystal systems is more complicated because these low-symmetry materials have quite different optical properties depending upon the orientation of their crystallographic axes, although in some cases, pressed pellets have been made to calculate orientation-averaged optical constants (Glotch et al., 2007; Roush et al., 1991). A method of using dispersion analysis and reflection spectra obtained at normal incidence to calculate the optical constants of monoclinic crystals was developed by Belousov and Pavinich (1978) and applied to spodumene (Pavinich & Belousov, 1978) and gypsum (Aronson et al., 1983). Although these works made great improvement in acquiring optical constants of low-symmetry crystals, they were restricted at simplified normal incident light. Mayerhöfer et al. (2011) provided more general formulas for the reflection from arbitrary angles of incidence based on the Berreman (1972) 4×4 matrix formulation and successfully applied the model to single crystal $K_2Ni(SO_4)_2 \bullet 6H_2O$ (Mayerhöfer et al., 2012). Arnold et al. (2014) determined the optical constants of several important monoclinic rock-forming minerals, including one alkali feldspar and four clinopyroxenes, following the method of Mayerhöfer et al. (2011).

The theory of the normal incidence reflection from triclinic crystals was developed by Emslie and Aronson (1983) adapting the method of Belousov and Pavinich (1978). The first result of applying dispersion analysis on a triclinic crystal of $CuSO_4 \bullet 5H_2O$ was presented by Aronson et al. (1985). Similar to their works on monoclinic crystals, they were limited to spectroscopic measurements at normal incidence. Höfer et al. (2013, 2014) applied dispersion analysis to triclinic crystals $CuSO_4 \bullet 5H_2O$ and $K_2Cr_2O_7$ with reflectance at arbitrary angles of incidence by the employment of a 4×4 matrix formulation (Berreman, 1972; Mayerhöfer & Popp, 2007; Yeh, 1980).

Based on these previous works, deriving optical constants of crystals from all symmetry systems becomes accessible by applying dispersion theory to reflectance measurements of minerals with arbitrary angles of incidence. However, optical constants for a variety of major rock-forming minerals from triclinic symmetry system, such as plagioclase feldspars, are not available. This work is the expansion of Arnold et al. (2014, 2015). In this work, we extend the MATLAB code from the monoclinic system of Arnold et al. (2014) to the triclinic case, which applies dispersion theory and non-normal incidence reflection data to derive the optical constants of triclinic rock-forming plagioclase minerals, using labradorite (an intermediate to calcic member of the plagioclase series with An# 50-70) as a case study.

2. Background

2.1. Plagioclase on the Moon, Mars, and Asteroids

2.1.1. Plagioclase on the Moon

Laboratory analyses of returned Apollo samples reveal that the ancient lunar highlands are dominated by the anorthosite, a rock type containing an average of 75–95% plagioclase with an An# of ~98, which is the primary source of support for the lunar magma ocean hypothesis (Smith et al., 1970; Warren, 1985, 1990; Wood et al., 1970). Among these anorthositic samples, ferroan anorthosite (FAN) is one of the major rock types, which is marked by its distinctive low Mg/(Mg+Fe) compared with other pristine lunar rocks (Dowty et al., 1974), while the other major rock type is a magnesian-rich rock first noted by Warner et al. (1976) and referred to as the Mg-suite. This geochemical bimodality of lunar anorthosites appears to imply two or more distinct series of magma evolution within a lunar magma ocean or different models to explain the formation mechanism of the lunar anorthosite crust (e.g., Longhi, 2003; Ohtake et al., 2012; Warren, 1985, 1990).

Apollo samples provide invaluable information for our understanding of lunar surface composition but are limited to six locations on the nearside of the Moon. Remote sensing is a powerful approach for investigating the composition type and distribution in a regional and global context. In a telescopic study, Spudis

et al. (1984) suggested the presence of anorthosite, not by the presence of a 1.25-μm band but by the lack of other mafic absorption bands. However, this spectral signature could also be interpreted as the result of shocked plagioclase (Spudis et al., 1984) or space weathering of immature anorthosite surfaces (Lucey, 2002). Clementine ultraviolet–visible (UVVIS) imaging data sets examined the central peaks of over 100 impact craters across the Moon and demonstrated that the lunar crust is extremely anorthositic (Tompkins & Pieters, 1999). In the past decade, high spectral and spatial resolution VNIR reflectance data sets from the SELENE Spectral Profiler (SP) and Multiband Imager (MI) and the Chandrayaan-1 Moon Mineralogy Mapper (M^3) have identified iron-bearing crystalline plagioclase with its characteristic ~1.25-μm absorption band in diverse regions on the Moon (Cheek et al., 2013; Donaldson Hanna et al., 2014; Matsunaga et al., 2008; Ohtake et al., 2009; Pieters et al., 2009). The Diviner Lunar Radiometer Experiment onboard the Lunar Reconnaissance Orbiter (LRO) is the first MIR instrument to provide global and regional silicate composition coverage maps of the Moon (Glotch et al., 2010; Greenhagen et al., 2010; Song et al., 2013). Donaldson Hanna et al. (2014) provided a global assessment of pure crystalline plagioclase across the Moon using M^3 and Diviner data sets and suggested that the plagioclase composition across the lunar highlands is relatively uniform, high in An#, and consistent with plagioclase compositions found in the FAN.

2.1.2. Plagioclase on Mars

Orbital observations of the Martian surface by the Thermal Emission Spectrometer (TES) onboard Mars Global Surveyor (MGS) identified two major distinct spectral units, Surface Type 1 and Type 2, in low-albedo regions on Mars (Bandfield et al., 2000; Christensen et al., 2000). Surface Type 1 has been interpreted as basalt (Bandfield et al., 2000), while Surface Type 2 has been interpreted in multiple ways, including basaltic andesite (Bandfield et al., 2000) or altered basalt (Kraft et al., 2003; Michalski et al., 2005; Wyatt & McSween, 2002). Regardless of which scenario is true for Surface Type 2, the spectral features of both Surface Type 1 and Type 2 are dominated by plagioclase. Martian surface mineralogy has been determined by linear deconvolution modeling of TES spectral data and categorized into several representative groups according to their spectral shapes, and these results have revealed substantial abundances of plagioclase across the Martian surface (Bandfield, 2002; Rogers et al., 2007; Rogers & Christensen, 2007). Further study of plagioclase compositions on Mars from TES spectral data has demonstrated that the average plagioclase of Martian Surface Type 1 and Type 2 is ~An_{60}, which may indicate little variation of plagioclase compositions in the upper Martian crust (Milam et al., 2004, 2007, 2010).

2.1.3. Plagioclase on the Asteroids

Spectral deconvolution of MIR emissivity spectra of Vesta obtained from the Mid-Infrared Asteroid Spectroscopy Survey (MIDAS) and the Infrared Space Observatory (ISO) provided good estimates of plagioclase and pyroxene abundances and confirmed that Vesta's surface is primarily composed of howardite or eucrite-like mineral assemblages that are heterogeneous across its surface (Donaldson Hanna & Sprague, 2009). Vesta's surface compositions revealed by the Visible and Infrared Spectrometer onboard the Dawn spacecraft mission confirmed and strengthened the link between Vesta and HED meteorites (De Sanctis et al., 2012). Quantitative mapping of minerals on Vesta's surface using Dawn Visible and Infrared Spectrometer data indicated that spectrally neutral components, perhaps plagioclase, may be prevalent on some portions of the northern hemisphere of Vesta (Li & Milliken, 2015).

Abundant plagioclase feldspar has also been identified in O-type asteroid 3628 Božněmcová using VNIR reflectance spectra by Cloutis et al. (2006). The spectrum of Božněmcová can be matched by an assemblage of clinopyroxene (~55–75%) and plagioclase feldspar (~20–33%), which would be broadly similar to angrite meteorites (Binzel et al., 2001; Cloutis et al., 2006). They suggested that Božněmcová could have formed by melting and differentiation under oxidizing conditions and probably represents an unsampled angrite-like body.

2.2. Theoretical Background

Dispersion theory describes the vibration of a crystal lattice as a collection of Lorentzian harmonic oscillators. It calculates the dielectric tensor ($\varepsilon_{x,y,z}$) of a single crystal using a set of dispersion parameters that represent the lattice oscillators. The number of elements in the dielectric tensor depends on the symmetry of the crystal. Since isotropic crystals have homogeneous structures, the dielectric tensor can be reduced to a scalar dielectric constant:

$$\varepsilon_{x,y,z} = \begin{pmatrix} \varepsilon & 0 & 0 \\ 0 & \varepsilon & 0 \\ 0 & 0 & \varepsilon \end{pmatrix}. \tag{1}$$

For uniaxial and orthorhombic crystals, three crystallographic axes are perpendicular to each other, and the principle axes are parallel to the crystallographic axes. As a consequence, the dielectric tensor takes on the diagonal form:

$$\varepsilon_{x,y,z} = \begin{pmatrix} \varepsilon_x & 0 & 0 \\ 0 & \varepsilon_y & 0 \\ 0 & 0 & \varepsilon_z \end{pmatrix}. \tag{2}$$

In a monoclinic crystal, one principle axis is parallel to the crystallographic b axis, while the other two are not parallel to the crystallographic a and c axes because the b axis is perpendicular to the a and c axes, but the a and c axes are not orthogonal. Therefore, the dielectric tensor of monoclinic crystals is composed of a 2×2 matrix and a single element:

$$\varepsilon_{x,y,z} = \begin{pmatrix} \varepsilon_{xx} & \varepsilon_{xy} & 0 \\ \varepsilon_{yx} & \varepsilon_{yy} & 0 \\ 0 & 0 & \varepsilon_{zz} \end{pmatrix}. \tag{3}$$

The mathematical framework for dispersion analysis of triclinic crystals was described by Höfer et al. (2013), which we summarize below for convenience. The three crystallographic axes in triclinic crystals are inclined relative to each other, so the dielectric tensor of triclinic crystals is represented as

$$\varepsilon_{x,y,z} = \begin{pmatrix} \varepsilon_{xx} & \varepsilon_{xy} & \varepsilon_{xz} \\ \varepsilon_{yx} & \varepsilon_{yy} & \varepsilon_{yz} \\ \varepsilon_{zx} & \varepsilon_{zy} & \varepsilon_{zz} \end{pmatrix}. \tag{4}$$

The optical constants of triclinic crystals are related to the dielectric tensor by

$$\begin{aligned} (n+ik)^2 &= \varepsilon_{x,y,z} \\ &= \begin{pmatrix} \varepsilon_{\infty,xx} & \varepsilon_{\infty,xy} & \varepsilon_{\infty,xz} \\ \varepsilon_{\infty,yx} & \varepsilon_{\infty,yy} & \varepsilon_{\infty,yz} \\ \varepsilon_{\infty,zx} & \varepsilon_{\infty,zy} & \varepsilon_{\infty,zz} \end{pmatrix} \\ &\quad + \sum_{j=1}^{N} \frac{s_j}{\nu_j^2 - i\gamma_j\nu - \nu^2} \times \begin{pmatrix} sin^2\theta_j cos^2\varphi_j & sin^2\theta_j sin\varphi_j cos\varphi_j & sin\theta_j cos\theta_j cos\varphi_j \\ sin^2\theta_j sin\varphi_j cos\varphi_j & sin^2\theta_j sin^2\varphi_j & sin\theta_j cos\theta_j sin\varphi_j \\ sin\theta_j cos\theta_j cos\varphi_j & sin\theta_j cos\theta_j sin\varphi_j & cos^2\theta_j \end{pmatrix}. \end{aligned} \tag{5}$$

Here, $\varepsilon_{\infty,x,y,z}$ is the high frequency dielectric tensor. The oscillator parameters include the resonant frequency (ν_j), the oscillator strength (s_j), damping coefficient (γ_j), and two angles (θ_j and φ_j) that represent the orientation of the oscillator's transition moment with respect to the crystal axes.

In order to properly apply dispersion analysis on a triclinic crystal, a cube cut out of a single crystal is required to ensure that the orientation of internal transition moments relative to the crystal surface can be clearly recognized to define the oscillator angles (θ_j and φ_j). The schematic geometry of the relative orientations of internal transition moments to the surfaces of a cube cut from the crystal is shown in Figure 1. In addition, the reflectance from diverse orientations of the cube surfaces relative to the direction of the polarized incoming beam needs to be measured. The orientations of the internal crystal axes with respect to the external laboratory coordinates are described by the Euler's angles Ω,Θ,Φ, given by

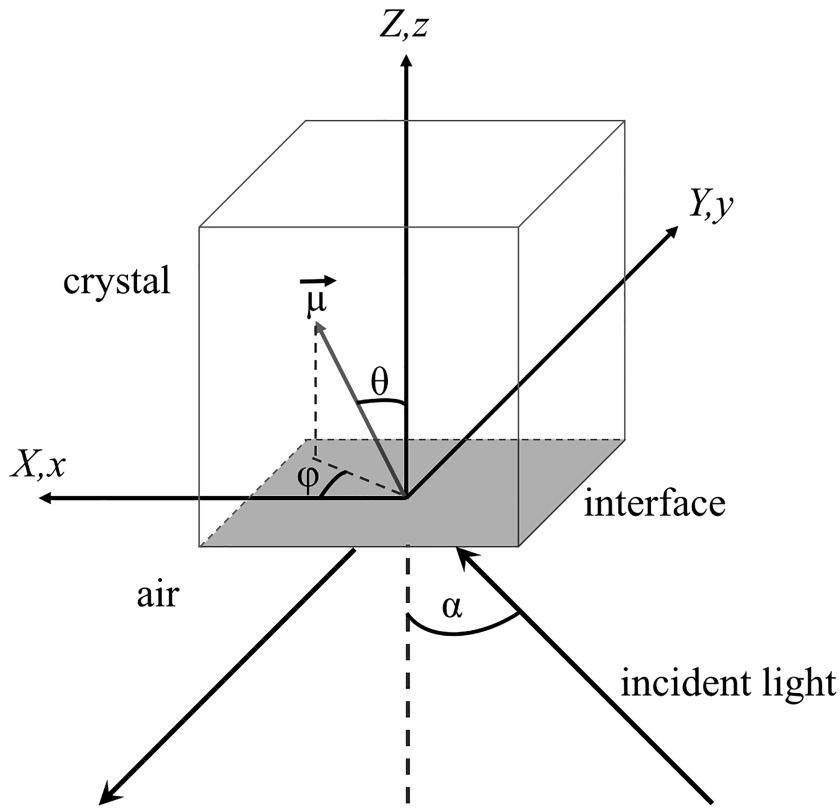

Figure 1. Schematic geometry of the reflectance measurements. The axes *X, Y,* and *Z* are the laboratory coordinate system. The interface between the sample and incident medium is parallel to the *X*-*Y* plane. The incident light propagates to the interface with an angle α. The orientation of internal transition moment $\vec{\mu}$ is described by the angles θ and φ relative to the intrinsic crystal coordinate system *x, y,* and *z*. This illustration is adapted from Höfer et al. (2013, 2014).

$$\varepsilon_{X,Y,Z} = \boldsymbol{A}(\Omega,\Theta,\Phi)\cdot\varepsilon_{x,y,z}\cdot\boldsymbol{A}^{-1}(\Omega,\Theta,\Phi). \tag{6}$$

$\boldsymbol{A}(\Omega,\Theta,\Phi)$ is the rotation matrix, defined as

$$\boldsymbol{A}(\Omega,\Theta,\Phi) = \boldsymbol{A}(\Phi)\cdot\boldsymbol{A}(\Theta)\cdot\boldsymbol{A}(\Omega), \tag{7}$$

$$\boldsymbol{A}(\Phi) = \begin{bmatrix} sin\Phi & -cos\Phi & 0 \\ cos\Phi & sin\Phi & 0 \\ 0 & 0 & 1 \end{bmatrix}, \tag{8}$$

$$\boldsymbol{A}(\Theta) = \begin{bmatrix} 1 & 0 & 0 \\ 0 & cos\Theta & sin\Theta \\ 0 & -sin\Theta & cos\Theta \end{bmatrix}, \tag{9}$$

$$\boldsymbol{A}(\Omega) = \begin{bmatrix} -sin\Omega & cos\Omega & 0 \\ -cos\Omega & -sin\Omega & 0 \\ 0 & 0 & 1 \end{bmatrix}, \tag{10}$$

$$\boldsymbol{A}(\Omega,\Theta,\Phi) = \begin{pmatrix} cos\ \Phi cos\ \Theta cos\Omega - sin\ \Phi sin\Omega & sin\ \Phi cos\Omega + cos\ \Phi cos\ \Theta sin\Omega & -cos\ \Phi sin\Theta \\ -cos\ \Phi sin\Omega - sin\ \Phi cos\ \Theta cos\Omega & cos\ \Phi cos\Omega - sin\ \Phi cos\ \Theta sin\Omega & sin\ \Phi sin\Theta \\ sin\ \Theta cos\Omega & sin\ \Theta sin\Omega & cos\Theta \end{pmatrix}. \tag{11}$$

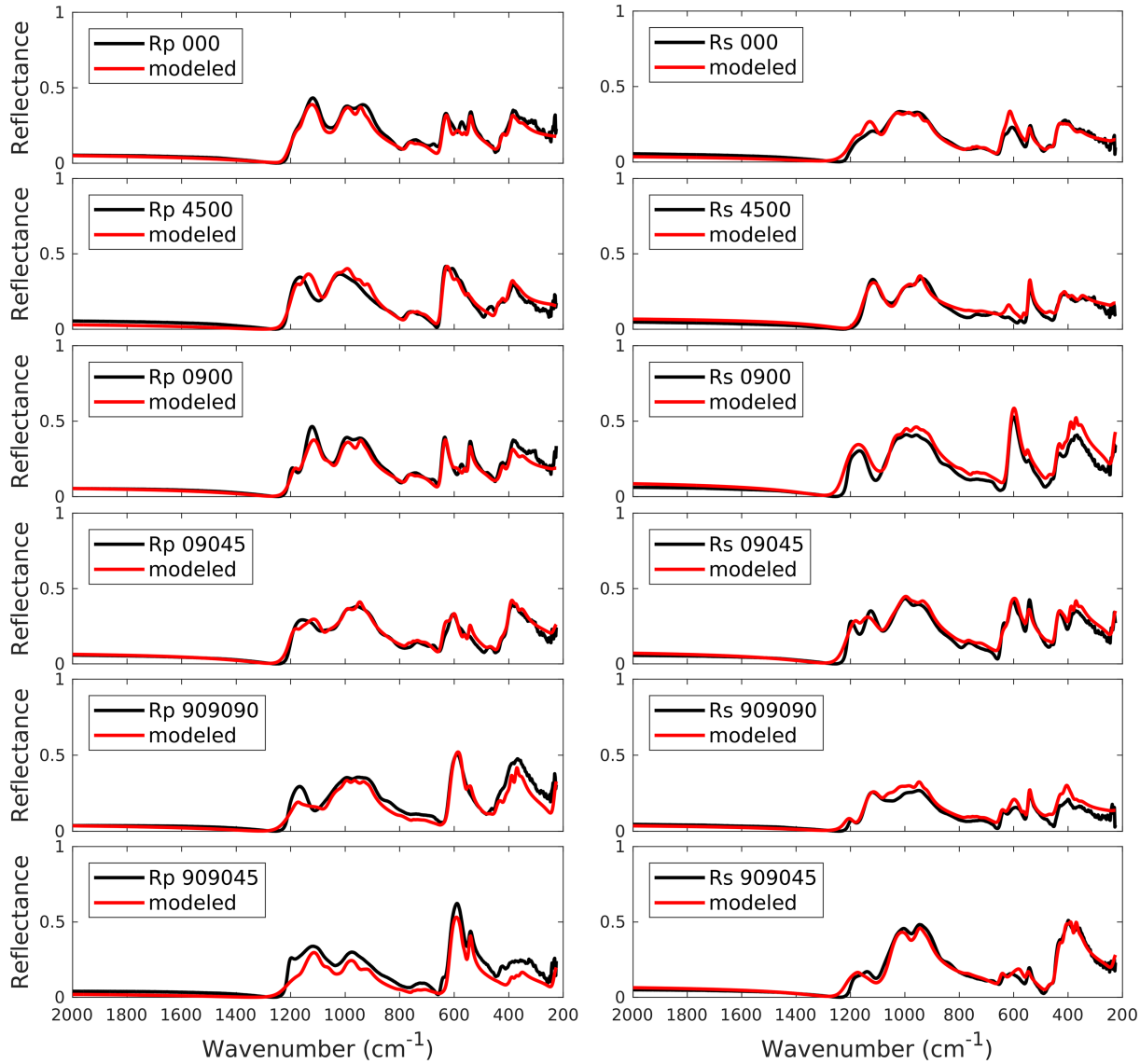

Figure 2. Measured and modeled reflectance spectra of labradorite with polarization directions perpendicular (R_s) and parallel (R_p) to the plane of incidence. Numbers in the legends are rotation angles in a fixed laboratory coordinate system following the nomenclature developed by Höfer et al. (2013) to represent different orientations of the labradorite crystal cube.

The rotation matrix $\boldsymbol{A}(\Omega)$, $\boldsymbol{A}(\Theta)$, and $\boldsymbol{A}(\Phi)$describes the rotation around the Z axis, X axis, and Z axis, respectively.

To calculate the reflectance from an anisotropic single crystal surface, a 4×4 matrix formalism is used, which was developed by Berreman (1972) and Yeh (1980), then generalized by Mayerhöfer and Popp (2007). Here we give a brief review of reflectance calculation for a triclinic crystal surface. In the reflectance measurement geometry as illustrated in Figure 1, the incident wave vector $\boldsymbol{k} = k_0(0, sin\alpha, cos\alpha)^T$ propagates onto a face of the triclinic crystal with an arbitrary angle α, and the continuity of electromagnetic field $\boldsymbol{\Psi} = (E_X, H_Y, E_Y, -H_X,)^T$ at the interface applying Maxwell's equation is

$$\frac{\partial}{\partial Z}\boldsymbol{\Psi} = ik_0\Delta\boldsymbol{\Psi}, \tag{12}$$

where Δ represents a 4×4 matrix:

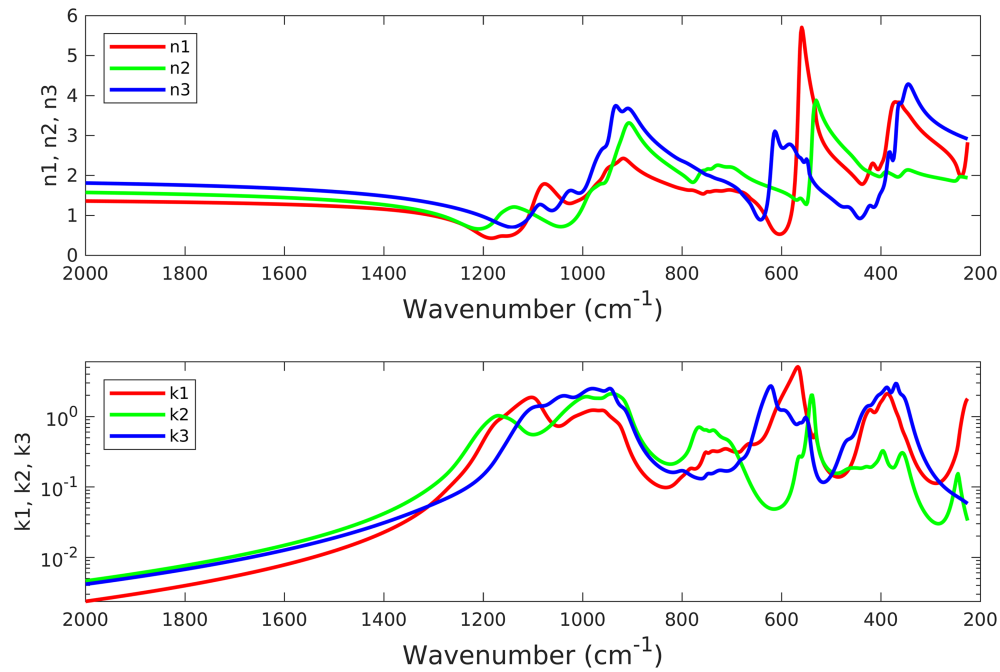

Figure 3. Optical constants of labradorite from three principle axes.

$$\Delta = \begin{pmatrix} 0 & 1 & 0 & 0 \\ k_Y^2 + \varepsilon_{XX} - \frac{\varepsilon_{XZ}{}^2}{\varepsilon_{ZZ}} & 0 & \varepsilon_{XY} - \frac{\varepsilon_{XZ}\varepsilon_{YZ}}{\varepsilon_{ZZ}} & -\frac{k_Y\varepsilon_{XZ}}{\varepsilon_{ZZ}} \\ -\frac{k_Y\varepsilon_{XZ}}{\varepsilon_{ZZ}} & 0 & -\frac{k_Y\varepsilon_{YZ}}{\varepsilon_{ZZ}} & 1 - \frac{k_Y^2}{\varepsilon_{ZZ}} \\ \varepsilon_{XY} - \frac{\varepsilon_{XZ}\varepsilon_{YZ}}{\varepsilon_{ZZ}} & 0 & \varepsilon_{YY} - \frac{\varepsilon_{YZ}{}^2}{\varepsilon_{ZZ}} & -\frac{k_Y\varepsilon_{YZ}}{\varepsilon_{ZZ}} \end{pmatrix}, \tag{13}$$

where k_Y is the Y-component of the incident wave vector, and a non-magnetic medium is assumed. The dynamical matrix of the incident wave is given by

$$\mathbf{D}_{\mathbf{\Psi}}^{-1}(0) = \begin{pmatrix} \frac{1}{2} & \frac{1}{2cos\alpha} & 0 & 0 \\ \frac{1}{2} & -\frac{1}{2cos\alpha} & 0 & 0 \\ 0 & 0 & \frac{1}{2cos\alpha} & \frac{1}{2} \\ 0 & 0 & -\frac{1}{2cos\alpha} & \frac{1}{2} \end{pmatrix}, \tag{14}$$

under the assumption that the index of refraction of the incident medium is 1. The dynamical matrix of the refracted wave in the crystal consists of two out of four eigenvectors of Δ matrix, which describes the forward traveling wave:

$$\mathbf{D}_{\mathbf{\Psi}}(1) = \begin{pmatrix} \Psi_{I,1} & 0 & \Psi_{II,1} & 0 \\ \Psi_{I,2} & 0 & \Psi_{II,2} & 0 \\ \Psi_{I,3} & 0 & \Psi_{II,3} & 0 \\ \Psi_{I,4} & 0 & \Psi_{II,4} & 0 \end{pmatrix}. \tag{15}$$

Table 1
Oscillator parameters for labradorite

j	ν_j	γ_j	s_j	φ_j	θ_j
1	221.84	22.224	56642	−179.98	8.6601
2	351.98	28.533	67337	73.013	41.863
3	354.14	27.305	74014	21.279	−6.0457
4	367.4	13.132	64986	−31.673	24.7
5	382.98	29.746	151510	100.23	70.521
6	385.85	14.882	41608	−34.118	25.759
7	401.09	23.272	44378	−12.406	57.257
8	420.76	20.643	27256	−69.625	75.586
9	425.34	22.268	13623	39.581	52.249
10	431.98	26.848	18320	−86.758	51.398
11	468.04	33.676	12097	33.267	34.032
12	537.14	11.205	74006	41.237	124.13
13	550.5	12.404	20706	93.01	−10.595
14	563.29	16.425	140580	−27.417	−39.583
15	563.57	13.081	226900	−55.731	−47.921
16	590.64	41.439	123820	−75.542	−113.41
17	617.97	16.734	121640	111.48	−79.001
18	670.9	98.566	41310	32.058	−30.936
19	708.24	45.085	47262	−53.823	−56.919
20	727.6	54.046	31816	87.991	−64.937
21	736.56	28.312	30940	−58.479	−61.479
22	751.06	12.539	5736.5	−55.75	−52.642
23	765.67	32.801	51386	108.73	−87.259
24	799.8	33.595	8738.3	−21.048	−19.94
25	913.72	35.305	183220	−74.075	−5.5842
26	916.54	31.896	189810	−53.89	81.6
27	930.53	32.499	155040	3.2489	7.7279
28	940.7	25.42	269570	−111.96	−66.599
29	942.62	34.891	109240	−42.873	73.619
30	961.41	34.548	160220	−44.961	−31.336
31	968.13	95.09	240540	−74.462	53.43
32	974.96	46.501	159110	−27.403	106.95
33	976.99	50.32	265840	−91.877	94.227
34	987.72	37.486	91761	38.216	7.4594
35	1003.9	61.557	110940	33.467	68.491
36	1031.9	53.384	227390	−52.021	−47.391
37	1085.4	64.586	15615	−9.8079	5.3716
38	1088.8	53.897	183270	44.185	−65.295
39	1092.5	44.303	180780	−82.913	107.52
40	1144.9	81.185	78423	−170.75	−13.717
41	1154.7	79.473	98913	−2.8591	5.2649
42	1168.4	27.91	13281	−53.861	47.102

$$\begin{pmatrix} \varepsilon_{\infty,xx} & \varepsilon_{\infty,xy} & \varepsilon_{\infty,xz} \\ \varepsilon_{\infty,yx} & \varepsilon_{\infty,yy} & \varepsilon_{\infty,yz} \\ \varepsilon_{\infty,zx} & \varepsilon_{\infty,zy} & \varepsilon_{\infty,zz} \end{pmatrix} = \begin{pmatrix} 2.0806 & 0.0031 & 0.0013 \\ 0.0031 & 3.6075 & 0.4293 \\ 0.0013 & 0.4293 & 3.2118 \end{pmatrix}$$

Note. The parameter ν_j is the resonant frequency, s_j is the oscillator strength, γ_j is the damping coefficient, θ_j and φ_j are two angles that represent the orientation of the oscillator's transition moment with respect to the crystal axes, and $\varepsilon_{\infty,x,y,z}$ is the high frequency dielectric tensor.

The transfer matrix $\widetilde{\boldsymbol{M}}$, which is constructed according to $\widetilde{\boldsymbol{M}} = \mathbf{D}_{\boldsymbol{\Psi}}^{-1}(0)\mathbf{D}_{\boldsymbol{\Psi}}$ (1), can link the amplitudes of the incident (A_s, A_p), reflected (B_s, B_p), and transmitted (C_s, C_p) wave as

$$\begin{pmatrix} A_s \\ B_s \\ A_p \\ B_p \end{pmatrix} = \begin{pmatrix} \widetilde{M}_{11}\widetilde{M}_{12}\widetilde{M}_{13}\widetilde{M}_{14} \\ \widetilde{M}_{21}\widetilde{M}_{22}\widetilde{M}_{23}\widetilde{M}_{24} \\ \widetilde{M}_{31}\widetilde{M}_{32}\widetilde{M}_{33}\widetilde{M}_{34} \\ \widetilde{M}_{41}\widetilde{M}_{42}\widetilde{M}_{43}\widetilde{M}_{44} \end{pmatrix} \cdot \begin{pmatrix} C_s \\ 0 \\ C_p \\ 0 \end{pmatrix}, \tag{16}$$

where s and p represent the polarization direction perpendicular and parallel to the plane of incidence, respectively. The reflectance coefficients are calculated by

$$r_{ss} = \frac{\widetilde{M}_{21}\widetilde{M}_{33} - \widetilde{M}_{23}\widetilde{M}_{31}}{\widetilde{M}_{11}\widetilde{M}_{33} - \widetilde{M}_{13}\widetilde{M}_{31}}, \tag{17}$$

$$r_{sp} = \frac{\widetilde{M}_{41}\widetilde{M}_{33} - \widetilde{M}_{43}\widetilde{M}_{31}}{\widetilde{M}_{11}\widetilde{M}_{33} - \widetilde{M}_{13}\widetilde{M}_{31}}, \tag{18}$$

$$r_{ps} = \frac{\widetilde{M}_{11}\widetilde{M}_{23} - \widetilde{M}_{21}\widetilde{M}_{13}}{\widetilde{M}_{11}\widetilde{M}_{33} - \widetilde{M}_{13}\widetilde{M}_{31}}, \tag{19}$$

$$r_{pp} = \frac{\widetilde{M}_{11}\widetilde{M}_{43} - \widetilde{M}_{41}\widetilde{M}_{13}}{\widetilde{M}_{11}\widetilde{M}_{33} - \widetilde{M}_{13}\widetilde{M}_{31}}, \tag{20}$$

where the first subscript index of the reflectance coefficient denotes the orientation of the polarizer, and the second denotes the orientation of the analyzer relative to the laboratory reference frame. Finally, the measured quantity, reflectance R_s, R_p is given by

$$R_s = |r_{ss}|^2 + |r_{sp}|^2, \tag{21}$$

$$R_p = |r_{ps}|^2 + |r_{pp}|^2. \tag{22}$$

3. Method

3.1. Sample Description and Preparation

The labradorite sample is a gem quality crystal from Chihuahua, Mexico and was assessed for purity using electron microprobe analyses and powder X-ray diffraction (Byrne et al., 2015; Ye & Glotch, 2019). Three arbitrary orthogonal faces were cut using a diamond saw and polished to a 1-μm roughness to eliminate scattering at the crystal surface, creating three faces whose edges were designated as x, y, and z.

3.2. Mid-Infrared Reflectance Spectra Measurements

MIR specular reflectance spectra from different faces of the cube were acquired on a Nicolet 6700 FTIR spectrometer equipped with a specular reflectance accessory with incidence and reflection angles of 30° at the Center for Planetary Exploration, Stony Brook University. A gold-coated front surface mirror was used as the reflectance standard. The spectrometer and sample chamber were purged of CO_2 gas and H_2O vapor. An InfraSpecs wire grid IR polarizer was placed in the beam path for collection of polarized reflectance spectra. The MIR spectra were acquired from 225–2,000 cm^{-1} using a CsI beamsplitter and an uncooled deuterated L-alanine doped triglycine sulfate (DLaTGS) detector. A total of 512 scans were acquired at 2-cm^{-1} spectral sampling to produce the spectrum. In order to find all values in the dielectric tensor, for each

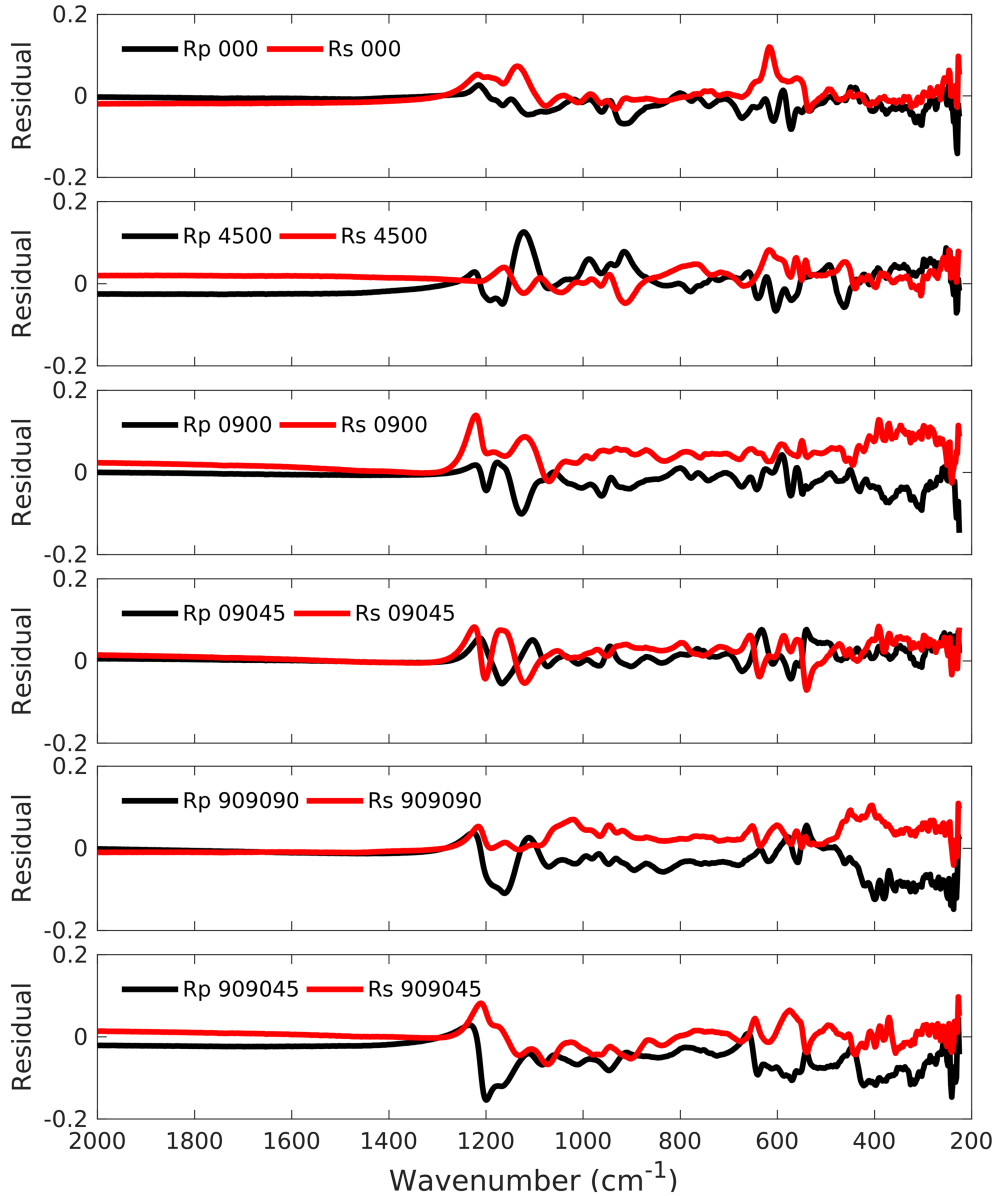

Figure 4. Residual difference between measured and modeled reflectance spectra of labradorite.

face, two spectra were acquired with the polarization direction parallel to each edge, and two additional spectra were acquired with the polarization direction along the diagonals of each face. Each spectrum was named according to a fixed laboratory coordinate system (X,Y,and Z) and the direction of polarization (s and p) following the nomenclature developed by Höfer et al. (2013).

3.3. Modeling of Optical Constants

The resulting 12 spectra were fit simultaneously with the modeled reflectance spectrum as we described above using a nonlinear least squares fitting routine in MATLAB. The infinite frequency dielectric constants were estimated from the square of previously measured visible values of the refractive index in the literature (Anthony et al., 1995). Initial guesses for the dispersion parameters were first found by modeling the spectra in the normal incidence case. These values were then iterated to refine the final values for the dispersion parameters. We set the lower and upper bounds for each parameter during the fitting to make sure the final values are positive. The optical constants were determined when the best fit was achieved with the minimum number of oscillators required.

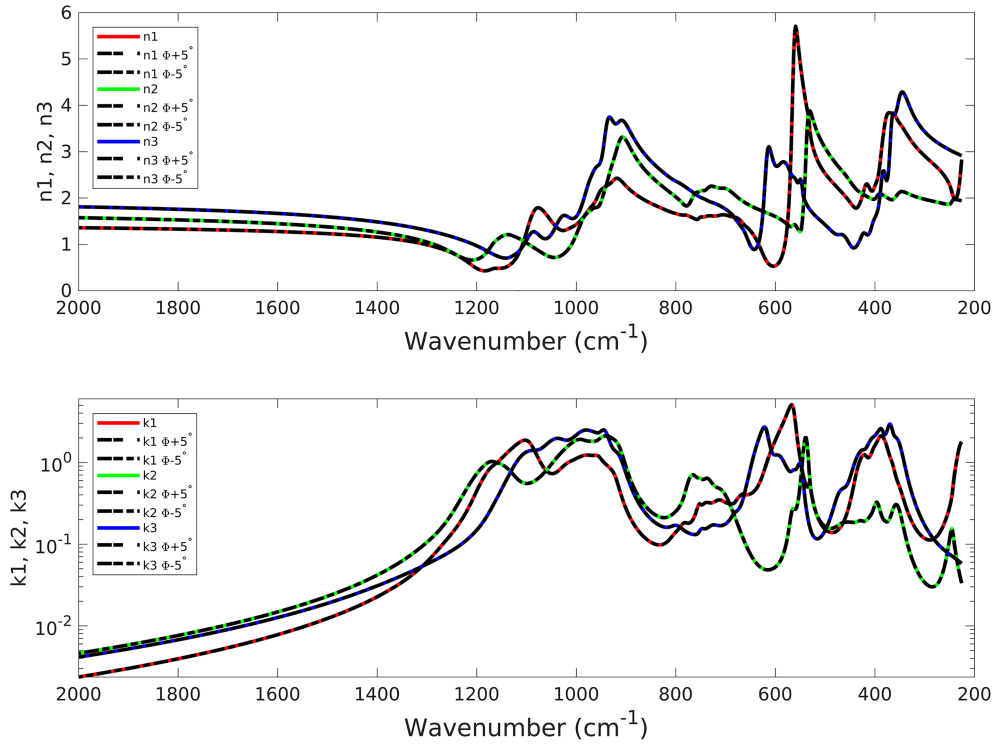

Figure 5. Derived optical constants with orientation variations by ±5°.

4. Results

Here we present the measured and modeled MIR reflectance and the derived values of n and k as a function of wavelength. Measured and modeled reflectances are shown in Figure 2, with multiple orientations and incident light polarization direction perpendicular and parallel to the surface. Derived values of n and k are shown in Figure 3. Oscillator parameters for this sample are given in Table 1.

5. Discussion

5.1. Model Discrepancies

Because of the complexity of the modeling procedures and large number of variables and data points, it is difficult to find a reasonable balance between the ideal fit and the required computation time. In general, the modeled spectra approximately match the positions and shapes of major peaks of the collected spectra, which are the primary features to characterize a spectrum. The major discrepancies between the measured and modeled spectra are observed at about 1,200 cm^{-1}, the 600 cm^{-1} region, and between 200 and 400 cm^{-1} (Figure 4). The 1,200 and 600 cm^{-1} areas are the resonance regions that show significant variations in reflectance spectra as expected because they are highly dependent on the sample orientation and light polarization, making it difficult to fit all the spectra simultaneously. The large errors between 200 and 400 cm^{-1} region for some of the spectra are likely due to the reduced signal to noise in the spectra caused by low transmission through the polarizer in this region and by the modeling difficulties at the end region of the wavelength range.

5.2. Error Analysis

The primary source of error is likely associated with the orientation of the sample during the spectral measurements. Therefore, the errors were estimated by using the same acquired laboratory spectra but modeling the reflectance using a Euler angle, $\Phi\pm5°$, and then evaluating the variation of the calculated optical constants. The results derived from misrepresentation of the sample orientations are displayed in Figure 5. They show that the orientation offsets do not affect the derived optical constants.

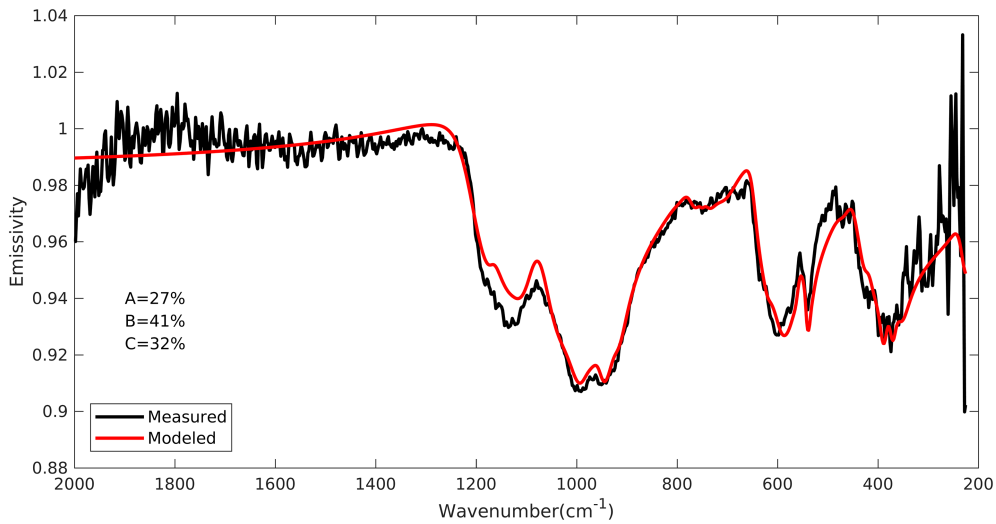

Figure 6. Comparison of measured and modeled emissivity spectra of coarse particulate labradorite. A, B, and C represent contributions of optical constants of principal indices a, b, and c, respectively.

5.3. Applications to MIR Spectral Modeling

For most applications of optical constants to planetary spectroscopy using radiative transfer theory, authors have used bulk optical constants instead of oriented optical constants to model spectra because the planetary surfaces are composed of particulates that have no preferred orientation. Therefore, we need to determine the average optical constants from three principle refractive indices. The contributions of optical constants from each principal axis were determined according to the method of Ito et al. (2017). We first measured the emissivity spectra of coarse particulate labradorite (>500 μm), the same sample that we used to derive the oriented optical constants, and then used a linear deconvolution method to fit the laboratory emissivity spectra using Fresnel reflectance (converted to emissivity via Kirchhoff's Law) calculated from three sets of optical constants as the library spectra. The fitting results generated contributions of 27, 41, and 32% from principal indices a, b, and c, respectively (Figure 6). This fitting result demonstrates the robustness of oriented optical constants we derived in this work.

6. Conclusion

We have derived the MIR (225–2,000 cm^{-1}) optical constants of a triclinic rock-forming plagioclase mineral, labradorite, using dispersion theory and a Fresnel reflectance model for the three principle crystal axes. This is the first attempt to acquire oriented MIR optical constants of a mineral in the triclinic plagioclase series. The deconvolution of the laboratory emissivity spectra of a coarse (>500 μm) particulate labradorite sample yields the relative contributions of optical constants from each principle axis required to represent the averaged optical constants that can be used to model randomly oriented spectra like might be present on a planetary surface based on radiative transfer theory. With the successful acquisition of optical constants of labradorite, we can expand this method to calculate optical constants of other triclinic plagioclase minerals.

Acknowledgments
This work is supported by NASA Solar System Workings award number NNX15AL55G to T. D. G., NSF award number AST-1150652 to T. D. G. and the RIS^{4}E node of NASA's Solar System Exploration Research Virtual Institute (T. D. G., PI). We are grateful to Darby Dyar for providing the labradorite sample. All data presented here will be archived at Stony Brook University Academic Commons repository (https://commons.library.stonybrook.edu/geodata/6). We thank Edward Cloutis and Melissa Lane for detailed reviews that improve the clarity of the manuscript.

References

Adams, J. B., & Goullaud, L. H. (1978). Plagioclase feldspars: Visible and near infrared diffuse reflectance spectra as applied to remote sensing, Proc. Lunar Planet. Sci. Conf., 9th, 2901-2909.

Anthony, J. W., Bideaux, R. A., Bladh, K. W., & Nichols, M. C. (1995). *Handbook of mineralogy*. Tucson, Arizona, USA: Mineral Data Publishing. 1995

Arnold, J. A., Glotch, T. D., & Plonka, A. M. (2014). Mid-infrared optical constants of clinopyroxene and orthoclase derived from oriented single crystal reflectance spectra. *American Mineralogist*, *99*(10), 1942–1955. https://doi.org/10.2138/am-2014-4828

Arnold, J. A., Rucks, M. J., & Glotch, T. D. (2015). Mid-IR optical constants of triclinic minerals. Lunar and Planetary Science Conference, 46th, abstract 2707.

Aronson, J. R., Emslie, A. G., Miseo, E. V., Smith, E. M., & Strong, P. F. (1983). Optical constants of monoclinic anisotropic crystals: Gypsum. *Applied Optics*, *22*(24), 4093–4098. https://doi.org/10.1364/AO.22.004093

Aronson, J. R., Emslie, A. G., & Strong, P. F. (1985). Optical constants of triclinic anisotropic crystals: Blue vitriol. *Applied Optics*, *24*(8), 1200–1203. https://doi.org/10.1364/AO.24.001200

Bandfield, J. L. (2002). Global mineral distributions on Mars. *Journal of Geophysical Research*, *107*(E6), 5042. https://doi.org/10.1029/2001JE001510

Bandfield, J. L., Hamilton, V. E., & Christensen, P. R. (2000). A global view of Martian surface compositions from MGS-TES. *Science*, *287*(5458), 1626–1630. https://doi.org/10.1126/science.287.5458.1626

Belousov, M. V., & Pavinich, V. F. (1978). Infrared reflection spectra of monoclinic crystals. *Optics and Spectroscopy*, *45*(5), 771–774.

Berreman, D. W. (1972). Optics in stratified and anisotropic media: 4x4-matrix formulation. *Journal of the Optical Society of America*, *62*(4), 502–510. https://doi.org/10.1364/JOSA.62.000502

Binzel, R. P., Harris, A. W., Bus, S. J., & Burbine, T. H. (2001). Spectral properties of near-earth objects: Palomar and IRTF results for 48 objects including spacecraft targets (9969) Braille and (10302) 1989 ML. *Icarus*, *151*(2), 139–149. https://doi.org/10.1006/icar.2001.6613

Byrne, S. A., Dyar, M. D., Bessette, E. E., Breitenfild, L. B., Crowley, M. C., Hoff, C. M., et al. (2015). Pure mineral separates for mixing experiments to simulate planetary surfaces. Lunar and Planetary Science Conference, 46th, abstract 1499.

Cheek, L. C., Donaldson Hanna, K. L., Pieters, C. M., Head, J. W., & Whitten, J. L. (2013). The distribution and purity of anorthosite across the Orientale basin: New perspectives from Moon Mineralogy Mapper data. *Journal of Geophysical Research: Planets*, *118*, 1805–1820. https://doi.org/10.1002/jgre.20126

Christensen, P. R., Bandfield, J. L., Smith, M. D., Hamilton, V. E., & Clark, R. N. (2000). Identification of a basaltic component on the Martian surface from Thermal Emission Spectrometer data. *Journal of Geophysical Research*, *105*(E4), 9609–9621. https://doi.org/10.1029/1999JE001127

Cloutis, E. A., Binzel, R. P., Burbine, T. H., Gaffey, M. J., & McCoy, T. J. (2006). Asteroid 3628 Božněmcová: Covered with angrite-like basalts? *Meteoritics & Planetary Science*, *41*(8), 1147–1161. https://doi.org/10.1111/j.1945-5100.2006.tb00512.x

Crown, D. A., & Pieters, C. M. (1987). Spectral properties of plagioclase and pyroxene mixtures and the interpretation of lunar soil spectra. *Icarus*, *72*(3), 492–506. https://doi.org/10.1016/0019-1035(87)90047-9

De Sanctis, M. C., Ammannito, E., Capria, M. T., Tosi, F., Capaccioni, F., Zambon, F., et al. (2012). Spectroscopic characterization of mineralogy and its diversity across Vesta. *Science*, *336*(6082), 697–700. https://doi.org/10.1126/science.1219270

Donaldson Hanna, K. L., Cheek, L. C., Pieters, C. M., Mustard, J. F., Greenhagen, B. T., Thomas, I. R., & Bowles, N. E. (2014). Global assessment of pure crystalline plagioclase across the Moon and implications for the evolution of the primary crust. *Journal of Geophysical Research: Planets*, *119*, 1516–1545. https://doi.org/10.1002/2013JE004476

Donaldson Hanna, K. L., & Sprague, A. L. (2009). Vesta and the HED meteorites: Mid-infrared modeling of minerals and their abundances. *Meteoritics & Planetary Science*, *44*(11), 1755–1770. https://doi.org/10.1111/j.1945-5100.2009.tb01205.x

Dowty, E., Prinz, M., & Keil, K. (1974). Ferroan anorthosite: Widespread and distinctive lunar rock type. *Earth and Planetary Science Letters*, *24*(1), 15–25. https://doi.org/10.1016/0012-821X(74)90003-X

Emslie, A. G., & Aronson, J. R. (1983). Determination of the complex dielectric tensor of triclinic crystals: Theory. *Journal of the Optical Society of America*, *73*(7), 916–919. https://doi.org/10.1364/JOSA.73.000916

Glotch, T. D., Christensen, P. R., & Sharp, T. G. (2006). Fresnel modeling of hematite crystal surfaces and application to Martian hematite spherules. *Icarus*, *181*(2), 408–418. https://doi.org/10.1016/j.icarus.2005.11.020

Glotch, T. D., Lucey, P. G., Bandfield, J. L., Greenhagen, B. T., Thomas, I. R., Elphic, R. C., et al. (2010). Highly silicic compositions on the Moon. *Science*, *329*(5998), 1510–1513. https://doi.org/10.1126/science.1192148

Glotch, T. D., & Rossman, G. R. (2009). Mid-infrared reflectance spectra and optical constants of six iron oxide/oxyhydroxide phases. *Icarus*, *204*(2), 663–671. https://doi.org/10.1016/j.icarus.2009.07.024

Glotch, T. D., Rossman, G. R., & Aharonson, O. (2007). Mid-infrared (5-100 μm) reflectance spectra and optical constants of ten phyllosilicate minerals. *Icarus*, *192*(2), 605–622. https://doi.org/10.1016/j.icarus.2007.07.002

Greenhagen, B. T., Lucey, P. G., Wyatt, M. B., Glotch, T. D., Allen, C. C., Arnold, J. A., et al. (2010). Global silicate mineralogy of the Moon from the Diviner lunar radiometer. *Science*, *329*(5998), 1507–1509. https://doi.org/10.1126/science.1192196

Höfer, S., Popp, J., & Mayerhöfer, T. G. (2013). Determination of the dielectric tensor function of triclinic $CuSO_4 \cdot 5H_2O$. *Vibrational Spectroscopy*, *67*, 44–54. https://doi.org/10.1016/j.vibspec.2013.04.003

Höfer, S., Popp, J., & Mayerhöfer, T. G. (2014). Dispersion analysis of triclinic $K_2Cr_2O_7$. *Vibrational Spectroscopy*, *72*, 111–118. https://doi.org/10.1016/j.vibspec.2014.03.003

Ito, G., Arnold, J. A., & Glotch, T. D. (2017). T-matrix and radiative transfer hybrid models for densely packed particulates at mid-infrared wavelengths. *Journal of Geophysical Research: Planets*, *122*, 822–838. https://doi.org/10.1002/2017JE005271

Kraft, M. D., Michalski, J. R., & Sharp, T. G. (2003). Effects of pure silica coatings on thermal emission spectra of basaltic rocks: Considerations for Martian surface mineralogy. *Geophysical Research Letters*, *30*(24), 2288. https://doi.org/10.1029/2003GL018848

Lane, M. D. (1999). Midinfrared optical constants of calcite and their relationship to particle size effects in thermal emission spectra of granular calcite. *Journal of Geophysical Research*, *104*(E6), 14,099–14,108. https://doi.org/10.1029/1999JE900025

Li, S., & Milliken, R. E. (2015). Quantitative Mapping of Minerals on Vesta Using Dawn VIR Data. Lunar and Planetary Science Conference, 46th, abstract 2179.

Longhi, J. (2003). A new view of lunar ferroan anorthosites: Postmagma ocean petrogenesis. *Journal of Geophysical Research*, *108*(E8), 5083. https://doi.org/10.1029/2002JE001941

Lucey, P. G. (2002). Radiative transfer model constraints on the shock state of remotely sensed lunar anorthosites. *Geophysical Research Letters*, *29*(10), 124. https://doi.org/10.1029/2001GL014655

Matsunaga, T., Ohtake, M., Haruyama, J., Ogawa, Y., Nakamura, R., Yokota, Y., et al. (2008). Discoveries on the lithology of lunar crater central peaks by SELENE Spectral Profiler. *Geophysical Research Letters*, *35*, L23201. https://doi.org/10.1029/2008GL035868

Mayerhöfer, T. G., Ivanovski, V., & Popp, J. (2012). Dispersion analysis of non-normal reflection spectra from monoclinic crystals. *Vibrational Spectroscopy*, *63*, 396–403. https://doi.org/10.1016/j.vibspec.2012.09.002

Mayerhöfer, T. G., & Popp, J. (2007). Employing spectra of polycrystalline materials for the verification of optical constants obtained from corresponding low-symmetry single crystals. *Applied Optics*, *46*(3), 327–334. https://doi.org/10.1364/ao.46.000327

Mayerhöfer, T. G., Weber, S., & Popp, J. (2011). Simplified formulas for non-normal reflection from monoclinic crystals. *Optics Communications*, *284*(3), 719–723. https://doi.org/10.1016/j.optcom.2010.10.003

Michalski, J. R., Kraft, M. D., Sharp, T. G., Williams, L. B., & Christensen, P. R. (2005). Mineralogical constraints on the high-silica martian surface component observed by TES. *Icarus*, *174*(1), 161–177. https://doi.org/10.1016/j.icarus.2004.10.022

Milam, K. A., McSween, H. Y., & Christensen, P. R. (2007). Plagioclase compositions derived from thermal emission spectra of compositionally complex mixtures: Implications for Martian feldspar mineralogy. *Journal of Geophysical Research: Planets*, *112*, E10005. https://doi.org/10.1029/2006JE002880

Milam, K. A., McSween, H. Y., Hamilton, V. E., Moersch, J. M., & Christensen, P. R. (2004). Accuracy of plagioclase compositions from laboratory and Mars spacecraft thermal emission spectra. *Journal of Geophysical Research: Planets*, *109*, E04001. https://doi.org/10.1029/2003JE002097

Milam, K. A., McSween, H. Y., Moersch, J., & Christensen, P. R. (2010). Distribution and variation of plagioclase compositions on Mars. *Journal of Geophysical Research: Planets*, *115*, E09004. https://doi.org/10.1029/2009JE003495

Nash, D. B., & Conel, J. E. (1974). Spectral reflectance systematics for mixtures of powdered hypersthene, labradorite, and ilmenite. *Journal of Geophysical Research*, *79*(11), 1615–1621. https://doi.org/10.1029/JB079i011p01615

Nash, D. B., & Salisbury, J. W. (1991). Infrared reflectance spectra (2.2-15 μm) of plagioclase feldspars. *Geophysical Research Letters*, *18*(6), 1151–1154. https://doi.org/10.1029/91GL01008

Ohtake, M., Matsunaga, T., Haruyama, J., Yokota, Y., Morota, T., Honda, C., et al. (2009). The global distribution of pure anorthosite on the Moon. *Nature*, *461*(7261), 236–240. https://doi.org/10.1038/nature08317

Ohtake, M., Takeda, H., Matsunaga, T., Yokota, Y., Haruyama, J., Morota, T., et al. (2012). Asymmetric crustal growth on the Moon indicated by primitive farside highland materials. *Nature Geoscience*, *5*(6), 384–388. https://doi.org/10.1038/ngeo1458

Pavinich, V. F., & Belousov, M. V. (1978). Dispersion analysis of reflection spectra of monoclinic crystals. *Optics and Spectroscopy*, *45*(6), 881–883.

Pieters, C. M., Boardman, J., Buratti, B., Clark, R., Combe, J. P., Green, R., et al. (2009). Mineralogy of the lunar crust in spatial context: First results from the Moon Mineralogy Mapper (M^3). Lunar and Planetary Science Conference, 40th, abstract 2052.

Ramsey, M. S., & Christensen, P. R. (1998). Mineral abundance determination: Quantitative deconvolution of thermal emission spectra. *Journal of Geophysical Research*, *103*(B1), 577–596. https://doi.org/10.1029/97JB02784

Rogers, A. D., Bandfield, J. L., & Christensen, P. R. (2007). Global spectral classification of Martian low-albedo regions with Mars Global Surveyor Thermal Emission Spectrometer (MGS-TES) data. *Journal of Geophysical Research: Planets*, *112*, E02004. https://doi.org/10.1029/2006JE002726

Rogers, A. D., & Christensen, P. R. (2007). Surface mineralogy of Martian low-albedo regions from MGS-TES data: Implications for upper crustal evolution and surface alteration. *Journal of Geophysical Research: Planets*, *112*, E01003. https://doi.org/10.1029/2006JE002727

Roush, T., Pollack, J., & Orenberg, J. (1991). Derivation of mid-infrared (5-25 μm) optical constants of some silicates and palagonite. *Icarus*, *94*(1), 191–208. https://doi.org/10.1016/0019-1035(91)90150-R

Rucks, M. J., & Glotch, T. D. (2014). Mid-IR optical constants of orthopyroxenes. AGU Fall Meeting, Abstract P23B-3987.

Salisbury, J. W., Walter, L. S., Vergo, N., & D'Aria, D. M. (1991). *Infrared (2.1-25 μm) spectra of minerals*, (p. 267). Baltimore: The Johns Hopkins University Press.

Smith, J. V., Anderson, A. T., Newton, R. C., Olsen, E. J., Crewe, A. V., Isaacson, M. S., et al. (1970). Petrologic history of the moon inferred from petrography, mineralogy and petrogenesis of Apollo 11 rocks. Proc. Apollo 11 Lunar Sci. Conf., 897-925.

Song, E., Bandfield, J. L., Lucey, P. G., Greenhagen, B. T., & Paige, D. A. (2013). Bulk mineralogy of lunar crater central peaks via thermal infrared spectra from the Diviner Lunar Radiometer: A study of the Moon's crustal composition at depth. *Journal of Geophysical Research: Planets*, *118*, 689–707. https://doi.org/10.1002/jgre.2006

Spitzer, W. G., & Kleinman, D. A. (1961). Infrared lattice bands of quartz. *Physical Review*, *121*(5), 1324–1335. https://doi.org/10.1103/PhysRev.121.1324

Spudis, P. D., Hawke, B. R., & Lucey, P. G. (1984). Composition of Orientale basin deposits and implications for the lunar basin-forming process. *Journal of Geophysical Research*, *89*(S01), C197–C210. https://doi.org/10.1029/JB089iS01p0C197

Tompkins, S., & Pieters, C. M. (1999). Mineralogy of the lunar crust: Results from Clementine. *Meteoritics & Planetary Science*, *34*(1), 25–41. https://doi.org/10.1111/j.1945-5100.1999.tb01729.x

Warner, J. L., Simonds, C. H. & Phinney, W. C. (1976). Genetic distinction between anorthosites and Mg-rich plutonic rocks: New data from 76255. Lunar and Planetary Science Conference, 7th, 915-917.

Warren, P. H. (1985). The magma ocean concept and lunar evolution. *Annual Review of Earth and Planetary Sciences*, *13*(1), 201–240. https://doi.org/10.1146/annurev.ea.13.050185.001221

Warren, P. H. (1990). Lunar anorthosites and the magma ocean plagioclase flotation hypothesis: Importance of FeO enrichment in the parent magma. *American Mineralogist*, *75*(1-2), 46–58.

Wenrich, M. L., & Christensen, P. R. (1996). Optical constants of minerals derived from emission spectroscopy: Application to quartz. *Journal of Geophysical Research*, *101*(B7), 15,921–15,931. https://doi.org/10.1029/96JB01153

Wood, J. A., Dickey Jr, J. S., Marvin, U. B., & Powell, B. N. (1970). Lunar anorthosites and a geophysical model of the moon. Proc. Apollo 11 Lunar Sci. Conf., 965-988.

Wyatt, M. B., & McSween, H. Y. (2002). Spectral evidence for weathered basalt as an alternative to andesite in the northern lowlands of Mars. *Nature*, *417*(6886), 263–266. https://doi.org/10.1038/417263a

Ye, C., & Glotch, T. D. (2019). Spectral properties of chloride salt-bearing assemblages: Implications for detection limits of minor phases in chloride-bearing deposits on Mars. *Journal of Geophysical Research: Planets*, *124*, 209–222. https://doi.org/10.1029/2018JE005859

Yeh, P. (1980). Optics of anisotropic layered media: A new 4x4 matrix algebra. *Surface Science*, *96*(1-3), 41–53. https://doi.org/10.1016/0039-6028(80)90293-9